1-1-2015

First-Principles Point Defect Models In Zr7ni10 And Zr2ni7 Binary Intermetallic Compounds And Their Implications In Nickel-Metal Hydride Batteries

Diana Felicia Wong
Wayne State University,

FIRST-PRINCIPLES POINT DEFECT MODELS IN Zr_7Ni_{10} AND Zr_2Ni_7 BINARY INTERMETALLIC COMPOUNDS AND THEIR IMPLICATIONS IN NICKEL-METAL HYDRIDE BATTERIES

by

DIANA F. WONG

THESIS

Submitted to the Graduate School

of Wayne State University,

Detroit, Michigan

in partial fulfillment of the requirements

for the degree of

MASTER OF SCIENCE

2015

MAJOR: CHEMICAL ENGINEERING

Approved By:

_____
Advisor   Date

DEDICATION

To my family and friends and their unconditional love and support.

ACKNOWLEDGMENTS

TABLE OF CONTENTS

v

LIST OF TABLES

LIST OF FIGURES

CHAPTER 1. INTRODUCTION

Of the over 9 million hybrid electric vehicles on the road worldwide today, most are powered primarily by nickel-metal hydride (Ni/MH) batteries. They offer excellent power performance under demanding conditions, operating reliably and safely upwards of 8-10 years through the cycles of summers and winters. They are also attractive for advanced start-stop applications, which hold incredible market potential with the increasing pressure from stricter government regulations worldwide to reduce fuel consumption and emissions in vehicles. Hybrid Ni/MH-lead-acid start-stop systems can extend service life to the lead-acid battery while boosting the vehicle's fuel economy [1]. Cost is also a major consideration factor for consumer vehicles, and rare-earth-free AB_2 Laves phase-based negative electrode active materials offer good electrochemical performance that can be tailored to specific applications at low cost potentials.

There are three major types of metal hydride (MH) alloys used in Ni/MH negative electrode active materials: AB_5, AB_2, and A_2B_7 alloys. Comparatively, AB_2 MH alloys have higher storage capacities and lower raw material costs but with tradeoffs to activation, high-rate dischargeability (HRD), and cycle durability [2]. However, the multi-phased nature of AB_2 Laves-phase-based MH alloys has enabled a dramatic increase in electrochemical performance in Ni/MH batteries, particularly with the inclusion of Zr-Ni-based secondary phases [3, 4]. The flexibility in chemical compositions, additives, and processing methods for AB_2 Laves-phase-based MH alloys and their effect on the structure and phase abundance characteristics have direct effects on electrochemical performance of these active materials to enable better activation, low-temperature performance, high-rate dischargeability (HRD), and cycle durability, through research and materials engineering [5].

Zr_7Ni_{10} is an important secondary phase found in multi-phased AB_2 Laves-phase-based MH alloys, and the synergetic effect between the Zr-Ni and the Laves phases allows access to the high hydrogen storage of the Zr-Ni phases despite the lower absorption/desorption kinetics [3, 4, 6, 7]. Zr_2Ni_7, on the other hand, has excellent absorption/desorption kinetics but poor hydrogen storage capacity [8]. Zr_7Ni_{10} shows solubility with Zr-rich stoichiometries, while Zr_2Ni_7 shows no solubility window. Stability of point defects within the crystal structure allows Zr_7Ni_{10} to maintain the same structure at off-stoichiometric compositions, thus it is theorized that defects may play a role in the difference between the electrochemical behaviors in Zr_7Ni_{10} and Zr_2Ni_7. Defects such as vacancies can act to trap hydrogen and inhibit the transport of hydrogen through the alloy [9]. Defects such as anti-sites can promote lower atomic packing ratios, which can improve cycling capability due to a higher propensity to deform rather than to crack [10, 11]. The ability to tune the ratio between hydride formers such as Zr and hydride modifiers such as Ni as well as to add other modifiers while maintaining the structure of the alloys is an important feature for designing battery materials targeting a specific application, and can strongly affect battery performance properties [5, 12-14].

The structure Zr_7Ni_{10} and its solubility window on the Zr-Ni binary phase diagram has been revised over the years and is a subject of contention [15-20]. First-principle calculations offer a theoretical method to evaluate the structure and study the defect models in these materials [21-24]. Defect models in Zr_7Ni_{10} and Zr_2Ni_7 computed using a combination of density functional theory (DFT) and statistical mechanics offer a starting point for understanding the nature of the Zr_7Ni_{10} secondary phases and their defects in Ni/MH batteries.

1.1 Objectives

This study has three major objectives in order to better understand the structure of constitutional defects in Zr_7Ni_{10} and Zr_2Ni_7 and how the defects may affect electrochemical performance in Ni/MH batteries:

1. To determine the ground state structure of Zr_7Ni_{10} by first principle calculations via DFT and confirm the structures found in experiment.

2. To determine the DFT formation energies of the compounds of interest, their defects, and of neighboring compounds to understand the relative ground state stability of the components at play in the Zr-Ni system at the compositions of interest.

3. To determine the relative constitutional defect concentrations and effective defect formation energies using a statistical mechanics model to preserve the overall alloy composition in Zr_7Ni_{10} and Zr_2Ni_7 compounds for stoichiometric and off-stoichiometric cases.

CHAPTER 2. BACKGROUND AND THEORY

2.1 Zr-Ni Binary Alloy System

The Zr-Ni binary phase diagram illustrates the different thermodynamically stable Zr-Ni phases that can form for a given composition of Zr and Ni at a specific temperature, and it is shown below in Figure 1. Zr_7Ni_{10} phase has an A/B stoichiometry ratio of 0.7, equivalent to 41.2% at. Zr. Studies originally showed Zr_7Ni_{10} phase with a solubility range that is hyperstoichiometric in Zr up to ~44% at. [18], but subsequent studies show a solubility range up to 41.5% at. maximum [19]. Phases such as Zr_2Ni_7 are "line compounds" and show no range in solubility.
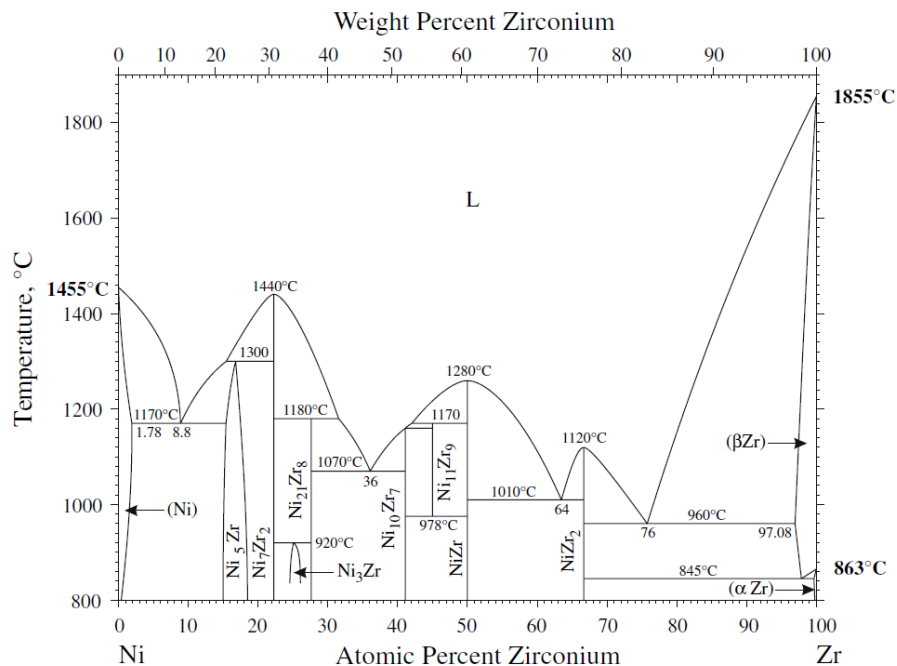
Figure 1. Zr-Ni binary phase diagram [20]

While processing methods, quenching techniques, and annealing methods can be used to obtain different phase mixtures for a given atomic composition, annealing at high temperature for a long period of time should yield the equilibrium phase or phases predicted by the binary

5

phase diagram. For example, off-stoichiometric ratios of Zr and Ni around 22.2% at. Zr melted together preferably forms a mixture of stoichiometric Zr_2Ni_7 and $ZrNi_5$ (if hypostoichiometric) or $ZrNi_3$ (if hyperstoichiometric) at equilibrium. It is the equilibrium structures that are of interest in this study.

The Zr-Ni system holds particular interest due to the role that Zr-Ni secondary phase plays in Laves phase-based electrodes used in Ni/MH batteries. Laves phase-based electrodes show good electrochemical capacity and offer a low cost alternative to expensive rare earth metal-based electrodes. While Zr_7Ni_{10} phase on its own performs relatively poorly, as a secondary phase, Zr_7Ni_{10} improves the surface transfer characteristics to provide a synergetic effect with the main Laves phase [3]. Zr_7Ni_{10} phase also has hydrogen storage capability in the electrodes, and further improvement in Zr_7Ni_{10} phase can boost the overall performance in Laves phase-based Ni/MH electrodes.

2.2 Defect Chemistry

Defects in crystalline materials fall under three major categories: point, linear, and planar defects [25]. Point defects are also known as constitutional defects. They are distributed throughout the bulk of the crystal and can exist at thermal equilibrium where linear and planar defects would be thermodynamically unstable [26]. Point defects can have a major effect on the thermodynamic, transport, and mechanical properties of materials, such as phase transition, diffusion, conductivity, plasticity, creep, and susceptibility to hydrogen embrittlement [9, 10, 21, 27]. The different types of point defects are the subject of study for Zr_7Ni_{10} and Zr_2Ni_7 compounds.

2.2.1 *Point Defects in Binary Ordered Compounds*

Zr_7Ni_{10} and Zr_2Ni_7 are binary, ordered intermetallic compounds with a specific structure and an ideal stoichiometry. Four major types of point defects are considered in this study:

1. Vacancies where normally a Ni atom occurs.

2. Vacancies where normally a Zr atom occurs.

3. Anti-site substitutions of a Zr atom where normally a Ni atom occurs.

4. Anti-site substitutions of a Ni atom where normally a Zr atom occurs.

Due to the size of the Zr and Ni atoms, interstitial defects, where an atom sits in a site where a vacancy normally occurs, are not considered in this study. Dumbbell interstitials, which can occur in alloys with Ni or Cu atoms [28, 29], are also neglected for the purposes of the model.

In a monatomic crystal, the energy of formation for point defects such as vacancies can be described as

$$\Delta H_v = E(N-1) - \frac{N-1}{N} E(N) ,$$

where ΔH_v is the energy of formation of a vacancy defect, $E(N)$ is the energy of the perfect crystal with N atoms, and $E(N-1)$ is the energy of the crystal with one vacancy defect [21]. These energies can be computed by DFT. Calculations using larger supercells reduce the interaction of the defects between adjacent cells and become more accurate.

The DFT model breaks down for non-monatomic systems such as the Zr_7Ni_{10} and Zr_2Ni_7 systems. Defect concentrations are temperature dependent, and increases to vacancy defects in a monatomic crystal does not change its composition. However, a Zr vacancy in ZrNi phase, for example, either generates an accompanying Ni vacancy or a Zr→Ni anti-site with a second Zr vacancy in order to maintain the 1:1 stoichiometry necessary for the phase. Other stoichiometries have different ratios of defects needed to maintain the stoichiometry. A

statistical mechanics model that uses energy parameters calculated by DFT can describe the distribution of point defects in binary ordered compounds and the effective energies for the defects to form.

2.3 Density Functional Theory

Density functional theory (DFT) has enabled the modeling of materials and their properties using quantum mechanical calculations with reasonable accuracy and speed. DFT takes the problem of many-body systems and maps its properties to a functional of the system's ground state density. The ground state density is a scalar function of position, and an approximate solution to the Schrödinger equation can be obtained for large many-bodied systems where direct numerical solutions involving the many-bodied wavefunction would be too resource-consuming to solve. Ref. [30] and [31] are excellent resources for understanding the background and theory behind computational chemistry and DFT, and this section relies on these two resources as well as the original journal sources for describing how DFT fits in the scope of this work.

2.3.1 Born-Oppenheimer Approximation

The Hamiltonian describes the kinetic and potential energies between interacting electrons and nuclei within a system of interest. Taking into account the kinetic energies and all Coulomb interactions (electron-nuclei, electron-electron, and nuclei-nuclei) yields

$$\widehat{H} = -\frac{\hbar^2}{2m_e}\sum_i \nabla_i^2 + \sum_{i,I} \frac{Z_I e^2}{|r_i - R_I|} + \frac{1}{2}\sum_{i\neq j} \frac{e^2}{|r_i - r_j|} - \sum_I \frac{\hbar^2}{2M_I}\nabla_I^2 + \frac{1}{2}\sum_{I\neq J} \frac{Z_I Z_J e^2}{|R_I - R_J|},$$

where lower case symbols denote electrons and upper case symbols denote nuclei for position vector r, mass m, electronic charge e, and nuclear charge Z_I [30]. The large difference in mass

8

between electrons and the nuclei leads to the Born-Oppenheimer approximation, in which the motion of the nuclei is essentially negligible compared to the motion of the electrons and the kinetic term for the nuclei can be largely ignored [32]. This simplifies the Hamiltonian, using Hartree atomic units, to

$$\hat{H} = \hat{T} + \hat{V}_{ext} + \hat{V}_{int} + E_{II} \,,$$

where $\hat{T}$ is the kinetic energy operator for the electrons,

$$\hat{T} = \sum_i -\frac{1}{2}\nabla_i^2 \,,$$

$\hat{V}_{ext}$ is the external potential from the nuclei acting on the electrons,

$$\hat{V}_{ext} = \sum_{i,I} V_I(|\mathbf{r}_i - \mathbf{R}_I|) \,,$$

$\hat{V}_{int}$ is the internal potential that arises from electron-electron interactions,

$$\hat{V}_{int} = \frac{1}{2}\sum_{i \neq j} \frac{1}{|\mathbf{r}_i - \mathbf{r}_j|} \,,$$

and E_{II} is the interaction between nuclei. The Born-Oppenheimer approximation allows the electronic motion to be separated from the atomic nuclei, which can now be viewed as an external potential acting on a collection of electrons.

2.3.2 Schrödinger Equation

The time-dependent Schrödinger equation governs the quantum state of a many-bodied system with respect to time by

$$i\hbar\frac{\partial}{\partial t}\Psi = \hat{H}\Psi \,,$$

where the Ψ is the wavefunction of the system [30]. Solutions of the time-independent Schrödinger equation

$$EΨ = \hat{H}Ψ \, ,$$

describe the wavefunctions that form stationary states (also known as "orbitals") for the system. The proportionality constant when the Hamiltonian operator acts on one of the stationary states is the energy, *E*, of the state. The total energy of the system is the expectation value of the Hamiltonian

$$E = \frac{\langle Ψ|\hat{H}|Ψ\rangle}{\langle Ψ|Ψ\rangle} = \langle \hat{H}\rangle = \langle \hat{T}\rangle + \langle \hat{V}_{\text{int}}\rangle + \int \mathrm{d}^3 r \, V_{\text{ext}}(r)\, n(r) + E_{II} \, ,$$

where the expectation value of the external potential has been rewritten in terms of the electron density *n*. The total energy of the system can be minimized to find the ground state wavefunction $Ψ_0$ of the system. It has an associated ground state density n_0.

2.3.3 *Thomas-Fermi-Dirac Approximation*

Thomas and Fermi first used a functional of density to approximate the electronic kinetic energy while neglecting the electron exchange and correlation interactions. Dirac included the exchange interactions in the energy functional

$$E_{\text{TF}}[n] = C_1 \int \mathrm{d}^3 r \, n(r)^{(5/3)} + \int \mathrm{d}^3 r \, V_{\text{ext}}(r) n(r) + C_2 \int \mathrm{d}^3 r \, n(r)^{(4/3)}$$

$$+ \frac{1}{2} \int \mathrm{d}^3 r \mathrm{d}^3 r' \, \frac{n(r) n(r')}{|r - r'|} \, ,$$

where C_1 and C_2 are known constants [30]. Minimizing the energy gives the ground state density and energy when subject to the constraint

$$\int \mathrm{d}^3 r \, n(r) = N.$$

The electron density can be viewed as the probability of finding electrons for a given space. For *N* indistinguishable electrons, the electron density is *N* times the probability of finding

an electron in the space. Compared to the traditional $3N$ degrees of freedom for N electrons required to determine the ground state wavefunction to find the ground state energy, Thomas, Fermi and Dirac laid the groundwork for DFT, reducing the requirements to finding the ground state energy to N degrees of freedom. However, their approximation considers the homogenous electron gas and oversimplifies aspects of inhomogeneous systems such as atoms and metals with impurities, which makes this method less useful for determining the electron structures needed to accurately model materials [33].

2.3.4 Hohenberg-Kohn Theorems

The theorems developed by Hohenberg and Kohn allow for an exact approach to density functional theory that applies to any system of interacting particles subject to an external potential, particularly the system of electrons and fixed nuclei described in Section 2.3.1 from the Born-Oppenheimer approximation. The theorems state [30, 33]:

1. Two external potentials $V_{ext}(\mathbf{r})$ and $V'_{ext}(\mathbf{r})$ with the same ground state density n_0 can only occur if $V'_{ext}(\mathbf{r}) - V_{ext}(\mathbf{r}) = \text{const}$, given that the ground states $\Psi_0 \neq \Psi'_0$.

   Corollary: This theorem leads to the inconsistency that $E + E' < E + E'$, which follows that the ground state density must uniquely determine the external potential (within a constant), thus determining all properties of the system.

2. For any system of N particles and any external potential $V_{ext}(\mathbf{r})$, there exists a universal functional $F[n]$ encompassing the kinetic and interaction energy such that $E[n] \equiv F[n] + \int d^3r\, V_{ext}(\boldsymbol{r})n(\boldsymbol{r})$. $E[n]$ is the global energy minimum, which is also the ground state energy, when $n(\boldsymbol{r})$ is exactly $n_0(\boldsymbol{r})$, the ground state electron density.

Corollary: This theorem shows that if $F[n]$ and the external potential are known, it is sufficient to determine the ground state energy and ground state density.

By the Hohenberg-Kohn theorems, then:

$$E_{\text{HK}}[n] = T[n] + E_{\text{int}}[n] + \int \mathrm{d}^3 r \, V_{\text{ext}}(\boldsymbol{r})n(\boldsymbol{r}) + E_{II} \equiv F_{\text{HK}}[n] + \int \mathrm{d}^3 r \, V_{\text{ext}}(\boldsymbol{r})n(\boldsymbol{r}) + E_{II} \,,$$

where $E_{\text{HK}} = E$, the exact energy of the system, and $F_{\text{HK}}[n]$ is the universal functional

$$F_{\text{HK}}[n] = T[n] + E_{\text{int}}[n] \,,$$

where $T[n]$ is the kinetic energy functional and $E_{\text{int}}[n]$ is the interaction energy functional. While the Hohenberg-Kohn theorems provide an exact approach to density functional theory to obtaining the ground state energy and density, the exact functionals are not known except for in certain, limiting cases that do not describe actual electronic systems.

2.3.5 Kohn-Sham Equations

The contributions that Kohn and Sham have made to density functional theory along with the advances in computing technology have enabled the widespread use of electronic structure calculations for the modeling of materials today. Their approach recasts the Hamiltonian that defines the many-bodied system into an auxiliary system that is more easily solved. The auxiliary independent particle Hamiltonian is defined as

$$\widehat{H}^{\sigma}_{\text{aux}} = -\frac{1}{2}\nabla^2 + V^{\sigma}_{\text{eff}}(\boldsymbol{r}) \,,$$

which consists of a non-interacting kinetic energy term and V^{σ}_{eff}, an effective local potential acting on an electron with spin σ [30, 34]. This rewrites the Hohenberg-Kohn energy functional to

$$E_{\text{KS}}[n] = T_{\text{s}}[n] + \int \mathrm{d}^3 r \, V_{\text{ext}}(\boldsymbol{r})n(\boldsymbol{r}) + E_{\text{Hartree}}[n] + E_{II} + E_{\text{xc}}[n] \,,$$

where T_s is the non-interacting kinetic energy, E_{Hartree} is the interaction energy of the electron density interacting with itself

$$E_{\text{Hartree}}[n] = \frac{1}{2}\int \mathrm{d}^3r\mathrm{d}^3r' \frac{n(\boldsymbol{r})n(\boldsymbol{r}')}{|\boldsymbol{r}-\boldsymbol{r}'|},$$

and E_{xc} captures the remaining exchange and correlation energy from the interacting particles. E_{xc} is thus defined as

$$E_{\text{xc}}[n] = F_{\text{HK}}[n] - (T_s[n] + E_{\text{Hartree}}[n]) = \langle \hat{T} \rangle - T_s[n] + \langle \hat{E}_{\text{int}} \rangle - E_{\text{Hartree}}[n],$$

which is the difference between the true kinetic and internal interaction energies of the interacting system with the energy of the independent, non-interacting system that has substituted the Hartree energy for the internal interaction energy. The effective local Kohn-Sham potential is finally defined as

$$V_{\text{eff}}^\sigma(\boldsymbol{r}) = V_{\text{ext}}(\boldsymbol{r}) + V_{\text{Hartree}}(\boldsymbol{r}) + V_{\text{xc}}^\sigma(\boldsymbol{r}).$$

There is a tradeoff with the Kohn-Sham approach. All of the terms are known exactly with the exception of E_{xc}, which can be approximated. However, obtaining T_s requires the treatment of orbitals rather than the density, which increases the degrees of freedom of the system back to $3N$. Approximation methods for E_{xc} make the tradeoff acceptable in terms of increased accuracy for the resource usage.

2.3.6 Exchange-Correlation Functionals

The functionals for approximating E_{xc} fall under three general classes: local density approximation (LDA), generalized gradient approximation (GGA) and hybrid functionals [30, 31]. The LDA method uses the density of a uniform electron gas integrated over all space to approximate the exchange-correlation energy. GGA methods improve upon the LDA method by incorporating the gradient of the density for each point in space, while requiring that the Fermi

13

and Coulomb hole properties be preserved. Hybrid methods construct functionals from a combination of LDA/GGA exchange-correlation functionals with the exact exchange energy functional from Hartree-Fock theory. Benchmarks for LDA and GGA methods show that GGA results (average absolute error 0.3 eV) improve bulk cohesive energy calculations over LDA results (average absolute error 1.3 eV) due to the underestimation of the exchange energy in the LDA [35]. Popular and successful GGA functionals have been proposed by Becke (B88) [36], Perdew-Wang (PW86, PW91) [37, 38], and Perdew-Burke-Ernzerhof (PBE) [39]. The PBE functional has found wide use in modeling materials, especially within the transition metal system, which makes it suitable for modeling Zr-Ni alloy materials.

2.3.7 *Ground State Structure and Energy of Formation*

A known external potential fixes the locations of the atoms within a specific structure. The energy of the specific configuration of atoms is determined when the energy within the DFT framework reaches a minimum over the iterations of the electron distribution and its structure. In order to find the equilibrium ground state structure for a system of interest, a minimization routine, typically a quasi-Newtonian algorithm, is used to iterate over atomic positions in until a minimum energy, zero forces, and zero stresses are reached. The relative stability of the ground state structures is defined by the energy of formation

$$\Delta H_f = \frac{E(A_n B_m) - \frac{n}{l} E(A_l) - \frac{m}{k} E(B_k)}{n + m},$$

where A_l and B_k are the constituent elemental compounds of the compound of interest $A_n B_m$. A_l and B_k, for example, may be of the forms body-centered cubic, face-centered cubic, hexagonal, etc, and l and k are the numbers of basis atoms in the respective unit cells.

2.4 Statistical Mechanics Model

Intrinsic point defects within an ordered binary system A_xB_{1-x} with fixed temperature at zero pressure are described within a generalized grand canonical ensemble [21, 22, 40, 41]. The number of atoms N_A and N_B fluctuate as a function of the independent variables temperature, volume, and chemical potentials μ_A and μ_B. The grand canonical potential is defined as

$$J = U - TS + PV - \mu_A N_A - \mu_B N_B ,$$

where U is the internal energy, T is the temperature, S is the entropy, P is the pressure, and V is the volume. The equilibrium concentrations of each type of point defect are found by minimizing the grand canonical potential with respect to the concentration or particle number of each type of defect. For M total lattice sites in the system consisting of A atoms on the α sublattice (with M^α total α sublattice sites) and B atoms on the β sublattice (with M^β total β sublattice sites), the total number of atoms are defined as

$$N_A = M^\alpha - N_B^\alpha - N_v^\alpha + N_A^\beta ,$$

$$N_B = M^\beta - N_A^\beta - N_v^\beta + N_B^\alpha ,$$

where $N_v^{\alpha,\beta}$ is the number of vacancies on the respective sublattice, N_B^α is the number of anti-sites on the α sublattice, and N_A^β is the number of anti-sites on the β sublattice. Multiple α and β sublattices may exist depending on the number of equivalent atoms in the unit cell. Each can have a different defect formation energy and should be accounted for similarly. The internal energy is defined as

$$U = M\varepsilon_0 + N_v^\alpha \varepsilon_v^\alpha + N_v^\beta \varepsilon_v^\beta + N_B^\alpha \varepsilon_B^\alpha + N_A^\beta \varepsilon_A^\beta ,$$

where ε_0 is the energy per unit cell of the system and ε_i^ν is the defect energy parameter for a defect of type i on a sublattice ν. The defect energy parameters are calculated by DFT for a supercell of size N such that

$$\varepsilon_0 = \frac{n}{N} E(N, 0),$$

$$\varepsilon_v^{\alpha,\beta} = E(N-1, 1^{\alpha,\beta}) - E(N, 0),$$

$$\varepsilon_A^{\beta} = E(N, A^{\beta}) - E(N, 0),$$

$$\varepsilon_B^{\alpha} = E(N, B^{\alpha}) - E(N, 0),$$

where *n* is the number of basis atoms in the elementary unit cell, $E(N, 0)$ is the ground state energy of the supercell of size N with zero defects, $E(N-1, 1^{\alpha,\beta})$ is the ground state energy of the supercell of size $N-1$ with one vacancy on the respective sublattice, $E(N, A^{\beta})$ is the ground state energy of the supercell of size N with one A atom on the β sublattice, and $E(N, B^{\alpha})$ is the ground state energy of the supercell of size N with one B atom on the α sublattice. The entropy is the statistical count of the configurations in the system (neglecting the formation entropy of the defects) given by

$$S = k_B \ln\left(\frac{M^{\alpha}!}{N_v^{\alpha}! N_B^{\alpha}! (M^{\alpha} - N_v^{\alpha} - N_B^{\alpha})!} \cdot \frac{M^{\beta}!}{N_v^{\beta}! N_A^{\beta}! (M^{\beta} - N_v^{\beta} - N_A^{\beta})!} \right).$$

where k_B is the Boltzmann constant. Substituting the equations into the expression for the grand canonical potential and minimizing with respect to the particle numbers yields the equilibrium concentrations of the defects

$$c_v^{\alpha} = \frac{N_v^{\alpha}}{M} = \frac{M^{\alpha}}{M} \frac{e^{-\beta(\varepsilon_v^{\alpha} + \mu_A + P v_v^{\alpha})}}{1 + e^{-\beta(\varepsilon_v^{\alpha} + \mu_A + P v_v^{\alpha})} + e^{-\beta(\varepsilon_B^{\alpha} + \mu_A - \mu_B + P v_B^{\alpha})}},$$

$$c_B^{\alpha} = \frac{N_B^{\alpha}}{M} = \frac{M^{\alpha}}{M} \frac{e^{-\beta(\varepsilon_B^{\alpha} + \mu_A - \mu_B + P v_B^{\alpha})}}{1 + e^{-\beta(\varepsilon_v^{\alpha} + \mu_A + P v_v^{\alpha})} + e^{-\beta(\varepsilon_B^{\alpha} + \mu_A - \mu_B + P v_B^{\alpha})}},$$

$$c_v^{\beta} = \frac{N_v^{\beta}}{M} = \frac{M^{\beta}}{M} \frac{e^{-\beta(\varepsilon_v^{\beta} + \mu_B + P v_v^{\beta})}}{1 + e^{-\beta(\varepsilon_v^{\beta} + \mu_B + P v_v^{\beta})} + e^{-\beta(\varepsilon_A^{\beta} + \mu_B - \mu_A + P v_A^{\beta})}},$$

$$c_A^\beta = \frac{N_A^\beta}{M} = \frac{M^\beta}{M} \frac{e^{-\beta\left(\varepsilon_A^\beta + \mu_B - \mu_A + Pv_A^\beta\right)}}{1 + e^{-\beta\left(\varepsilon_v^\beta + \mu_B + Pv_v^\beta\right)} + e^{-\beta\left(\varepsilon_A^\beta + \mu_B - \mu_A + Pv_A^\beta\right)}}.$$

The chemical potentials can be obtained from the thermodynamic relations such that

$$N_A = \frac{\partial J}{\partial \mu_A},$$

$$N_B = \frac{\partial J}{\partial \mu_B},$$

which gives the expression

$$\varepsilon_0 + Pv_0 = \frac{M^\alpha}{M}\mu_A + \frac{M^\beta}{M}\mu_B - \frac{M^\alpha}{M}k_BT \ln\left(1 - \frac{M}{M^\alpha}c_v^\alpha - \frac{M}{M^\alpha}c_B^\alpha\right)$$

$$- \frac{M^\beta}{M}k_BT \ln\left(1 - \frac{M}{M^\beta}c_v^\beta - \frac{M}{M^\beta}c_A^\beta\right),$$

and then imposing the restriction

$$\frac{N_A}{N_B} = \frac{M^\alpha - N_B^\alpha - N_v^\alpha + N_A^\beta}{M^\beta - N_A^\beta - N_v^\beta + N_B^\alpha} = \frac{x}{1-x},$$

in order to maintain the correct composition of the system.

The effective formation energy of the atomic defects is defined as

$$\Delta H_i^\nu = -k_B \frac{\partial c_i^\nu}{\partial\left(\frac{1}{T}\right)},$$

which is simplified as

$$\Delta H_i^\nu = \varepsilon_i^\nu - \delta_{i,A}\mu_A + \delta_{v,A}\mu_A - \delta_{i,B}\mu_B + \delta_{v,B}\mu_B,$$

where

$$\Delta H_v^\alpha = \varepsilon_v^\alpha + \mu_A,$$

$$\Delta H_v^\beta = \varepsilon_v^\beta + \mu_B,$$

$$\Delta H_B^\alpha = \varepsilon_B^\alpha - \mu_B + \mu_A,$$

$$\Delta H_A^\beta = \varepsilon_A^\beta - \mu_A + \mu_B \,.$$

It describes the energy required to overcome the barriers to the formations of defects while accounting for the same number of A and B atoms in the system [40]. It is dependent on temperature through the chemical potentials, as well as on the properties of the point defects within the system [41].

A number of assumptions simplifies the system of equations in order to numerically calculate the defect concentrations for the binary system. For systems at equilibrium volume, the pressure is taken to be zero. The contributions from vibrational energy and formation entropy are neglected due to the difficulty in calculating these quantities using *ab initio* methods. When defect concentrations are very small, the denominator in the concentration expressions can be approximated as unity. These assumptions can have a large effect on the interpretation of the effective formation energies if care is not taken. This method has been utilized in literature to study defects in a wide range of intermetallic compounds including FeAl, NiAl, NiAl₃, and TiNi with good correlation to experiment [21, 40, 42-45].

CHAPTER 3. POINT DEFECT MODELS IN Zr$_7$Ni$_{10}$ AND Zr$_2$Ni$_7$ BINARY

 INTERMETALLIC COMPOUNDS

Zr$_7$Ni$_{10}$ phase has an orthorhombic structure and sometimes occurs as a metastable

tetragonal phase [6, 19, 46]. It was originally reported to have space group symmetry *Aba2* [15,

16] and has since been revised to have space group symmetry *Cmca* [17]. Its crystal structure is

shown in Figure 2 below, rendered using VESTA graphical software [47]. It contains 68 atoms

per unit cell (*Z* = 4) with experimental parameters *a* = 12.381 Å, *b* = 9.185 Å, and *c* = 9.221 Å

[17]. The unit cell contains 4 equivalent Zr atoms in the 4*a*, 8*d*, 8*e* and 8*f* positions and 3

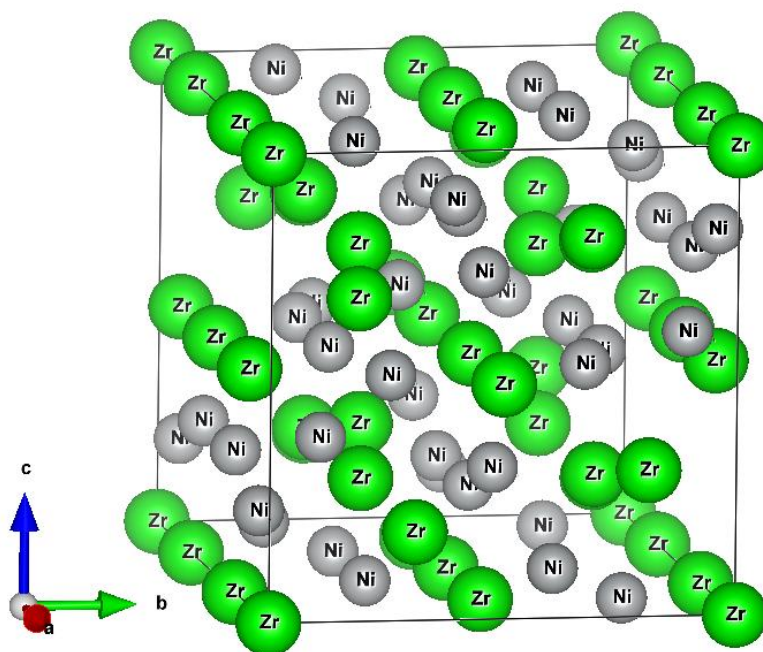equivalent Ni atoms in the 8*f* and 16*g* positions.

Figure 2. Zr$_7$Ni$_{10}$ crystal structure

Due to computational resources, we choose to investigate a combination of defects in one

8*d* and one 8*e* position for the Zr sublattices and one 16*g* position for the Ni sublattices for a total

of 6 defect structures. The lowest energy of the sublattice defects was considered for the

remaining equivalent sites. It is possible that the other sites may have different defect energies, which can affect the results, which we analyze with a sensitivity analysis. However, we lay the groundwork for theoretical analysis of point defects for the Zr_7Ni_{10} and Zr_2Ni_7 systems with this work. We also confirm computationally that Zr_7Ni_{10} phase relaxes to an equilibrium structure with space group *Cmca*.

Zr_2Ni_7 phase is monoclinic, and its crystal structure is shown in Figure 3 below. It contains 36 atoms per unit cell ($Z = 4$) with experimental parameters $a = 4.698$ Å, $b = 8.235$ Å, $c = 12.193$ Å and $\beta = 95.83°$ [48]. It contains 2 equivalent Zr atoms in the 4i positions and 4 equivalent Ni atoms in the 4i and 8j positions. Due to computational resources, we choose to investigate a combination of defects in one 4i position for Zr atoms and one 4i and one 8j position for Ni atoms for a total of 6 defect structures. We assume that the remaining equivalent atoms have similar energies to the atoms with similar Wyckoff positions.
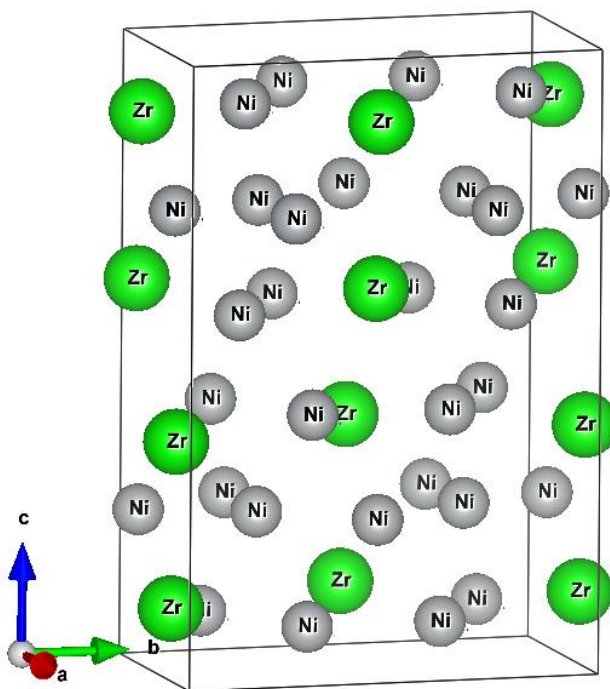

Figure 3. Zr₂Ni₇ crystal structure

3.1 Computational Methods

Electronic structure calculations were performed using the plane-wave-based density functional theory code implemented in Quantum Espresso [49] and ultra-soft pseudopotentials from the GBRV pseudopotential library [50]. The exchange-correlation potential applied the PBE version of the generalized gradient approximation [39]. The recommended plane-wave cutoff energy of 40 Ry and charge-density cutoff energy of 120 Ry allowed convergence within 1×10^{-5} Ry/atom of the energy. A Methfessel-Paxton smearing width of 0.02 Ry with a Monkhorst-Pack k-point grid that yields 100-200 k-points also met convergence criteria with reasonable speed [51, 52]. Spin-polarization was not included in the calculations due to the large size of the systems.

Cell structural optimizations for a given composition and structure were conducted by a variable cell relaxation calculation that minimizes forces and stresses within the cell. The cell is considered optimized when forces were below 1×10^{-3} Ry/Å, the minimum energy was converged to below 1×10^{-5} Ry/atom, and stresses converged within 0.5 kbar.

Zr_7Ni_{10} contains 68 atoms per unit cell. A supercell was not constructed due to the inherent large size of the cell. The structure with the space group *Aba2* was evaluated for the calculation and allowed to relax. Point defects involving select equivalent sites of the optimized structure were investigated. Zr_2Ni_7 contains 36 atoms per unit cell, and a $2\times1\times1$ supercell containing 72 atoms was constructed to reduce interactions of the defects in adjacent cells. Point defects involving select equivalent sites were investigated. Structures for $ZrNi_5$, Zr_8Ni_{21}, and ZrNi were also calculated to provide tie lines for the formation energy diagrams.

The statistical mechanics method for defects in ordered binary compounds was calculated using fsolve from the SciPy library for Python. The defect concentrations and effective

formation energies were calculated at a reference temperature of 1000°C, a temperature near the melting points for the Zr_7Ni_{10} and Zr_2Ni_7 systems. When precision limitations were encountered in Python (typically at low temperature, which results in extremely low defect concentrations), the logarithmic terms containing defect concentration variables were analyzed and dropped when low concentration assumptions were valid.

3.2 Theoretical Point Defects in Zr_7Ni_{10}

DFT calculation of Zr_7Ni_{10} phase in the space group *Aba2* results in a relaxed structure having space group *Cmca* symmetry. The calculated lattice parameters are shown in Table 1 below with comparative lattice parameters from experiment. The lattice parameters show reasonable agreement with experiment, although the calculated structure appears to converge to a near tetragonal unit cell. The tetragonal phase is considered a metastable phase, and it is observed after hydrogenation of the alloy, particularly in Ni/MH battery negative electrodes [6, 19, 46]. Defects in Zr_7Ni_{10} may play an important role in facilitating the phase change, as well as in promoting diffusion kinetics for improved rate performance and access to hydrogen storage capacity. The DFT defect formation energies for Zr_7Ni_{10} phase are calculated based on this optimized calculated structure.

Table 1. Zr_7Ni_{10} unit cell lattice parameters

	This Work	Ref. [16]	Ref. [17]
S.G.	*Cmca*	*Aba2*	*Cmca*
a (Å)	12.419	12.386	12.381
b (Å)	9.179	9.156	9.185
c (Å)	9.180	9.211	9.221

3.2.1 DFT Defect Formation Energies

Ground state DFT formation energies (at $T = 0K$) for Zr_7Ni_{10} phase and the theoretical Ni→Zr anti-site, Zr vacancy, Ni vacancy and Zr→Ni anti-site defects are plotted in Figure 4 with the tie lines to the neighboring compounds Zr_8Ni_{21} and ZrNi. All of the defect energies at 0K for the specific structures considered lie above the stoichiometric compound as well as above the tie lines, indicating energy is required for the defects to form, and that the defects are in competition with formation of phases or mixtures of phases. There is a large difference between the Zr sublattice sites investigated. This indicates that defects more preferentially form on the 8e sublattice than the 8d sublattice for Zr.

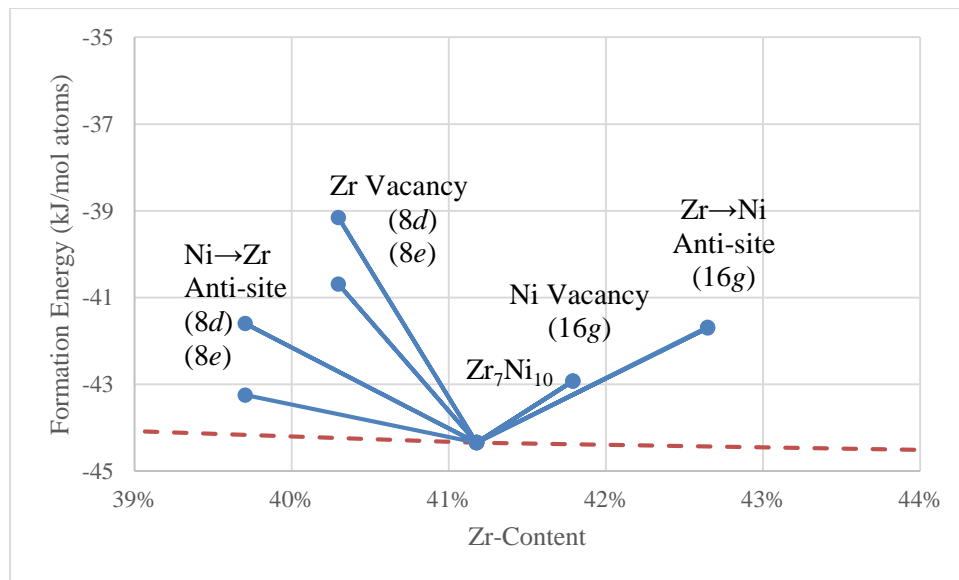*Figure 4. Formation energies for Zr_7Ni_{10} and its point defects with tie lines*

The model neglects temperature effects showing the effects of the heat of mixing, entropy, vibrational energy and defect interaction on the free energy of each of the possible phases, which is necessary for a more conclusive study of phase stability and solubility windows. However, the

DFT formation energies indicate that out of the defects considered, the 8e Ni→Zr anti-site defect and the Ni vacancy defect are the most stable of the point defects for Zr_7Ni_{10} phase. But since Zr_7Ni_{10} phase is an ordered, binary compound, a mixture of all point defects is necessarily generated in order to maintain the required stoichiometry, and this is addressed by the statistical mechanics model.

3.2.2   Theoretical Effective Formation Energies

The theoretical defect concentrations for Zr_7Ni_{10} phase at 1000°C calculated using the defect energy parameters derived from DFT electronic structure calculations are plotted as functions of Zr-content for stoichiometric and theoretical off-stoichiometric compositions in Figure 5. The solubility window for Zr_7Ni_{10} phase is reported to be at most 41.4% at. Zr-content [19]. Concentrations of defects on each of the different site sublattices were generated and added together to give a total concentration for a defect on the atomic sublattice. The A atoms represent Zr and the B atoms represent Ni in the statistical mechanics model, where c_v^α is the concentration of vacancies on the Zr sublattices, c_v^β is the concentration of vacancies on the Ni sublattices, c_B^α is the concentration of total Ni→Zr anti-site defects, and c_B^β is the concentration of total Zr→Ni anti-site defects.
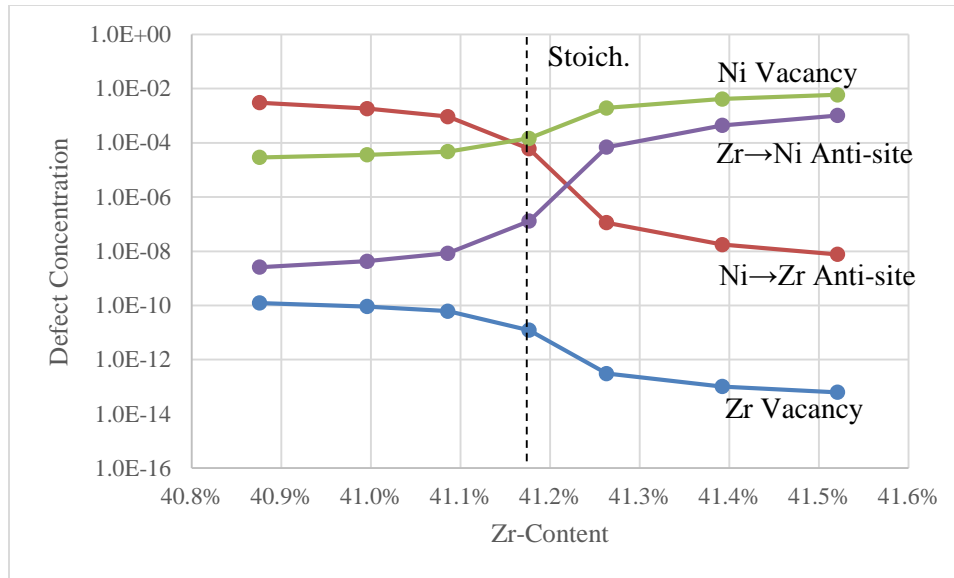
Figure 5. Theoretical defect concentrations for Zr₇Ni₁₀ at 1000°C

Stoichiometric Zr_7Ni_{10} phase at 1000°C is dominated by Ni vacancies and Ni→Zr anti-site defects at an approximately 2.4:1 ratio, indicating a defect structure possibly similar to a triple defect. Zr-rich compositions promote more defects on the Ni sublattices, with Ni vacancies outnumbering the Zr→Ni anti-site defects. Ni-rich compositions theoretically would promote defects on the Zr sublattices. Ni→Zr anti-site defects dominate in the analysis, and while the concentration of Zr vacancies increases, it does not approach the concentrations of the other defects. Each of the site lattices generated an effective formation energy, and a weighted average by the concentration of sites was used to calculate the theoretical effect formation energies of the atomic point defects. The theoretical effective formation energies for the respective point defects at 1000°C are tabulated in Table 2 and show the relative ease for which the defects can form. The effective formation energies for the defects are consistent with the defect concentration trends observed in Figure 5, with Ni vacancies showing the lowest effective formation energy at stoichiometry and on the Zr-rich side.

Table 2. Theoretical effective formation energies for point defects in Zr_7Ni_{10} at 1000°C

	ΔH_v^{α} (eV)	ΔH_v^{β} (eV)	ΔH_B^{α} (eV)	ΔH_A^{β} (eV)
Ni-rich	2.39	1.09	0.52	2.11
Stoich.	2.64	0.91	0.95	1.68
Zr-rich	3.22	0.51	1.94	0.70

3.3 Theoretical Point Defects in Zr_2Ni_7

The DFT structure optimization calculation for Zr_2Ni_7 phase is consistent with the monoclinic *C2/m* symmetry and structure reported in literature. The calculated lattice parameters are shown in Table 3 below with comparative lattice parameters from experiment. The lattice parameters show reasonable agreement with experiment. The DFT defect formation energies for Zr_2Ni_7 phase are calculated based on this optimized calculated structure.

Table 3. Zr_2Ni_7 unit cell lattice parameters

	This Work	Ref. [48]
a (Å)	4.677	4.698
b (Å)	8.239	8.235
c (Å)	12.176	12.193
β (°)	95.20	95.83

3.3.1 DFT Formation Energies

Ground state DFT formation energies for Zr_2Ni_7 phase and its theoretical Ni→Zr anti-site, Zr vacancy, Ni vacancy and Zr→Ni anti-site defects are plotted in Figure 6 with the tie lines to neighboring compounds $ZrNi_5$ and Zr_8Ni_{21}. All defects energies at 0K lie above the stoichiometric compounds as well as the tie lines. However, the Ni→Zr anti-site defect energy lies considerably higher than the stoichiometric compound than for the $ZrNi_5$-Zr_2Ni_7 mixture tie line, indicating a possible shift in the dominating defects found in a theoretical Ni-rich off-stoichiometric compound. The Zr→Ni anti-site defect energy is the lowest of the defects for

Zr₂Ni₇ phase, followed by the Ni vacancy defect energy. There is a small difference in defect energy between 4i and 8j sites for the Ni vacancy, but a much larger difference between the sites for the Zr→Ni anti-site defect. In general, point defects appear to prefer to form on the 8j sublattices.
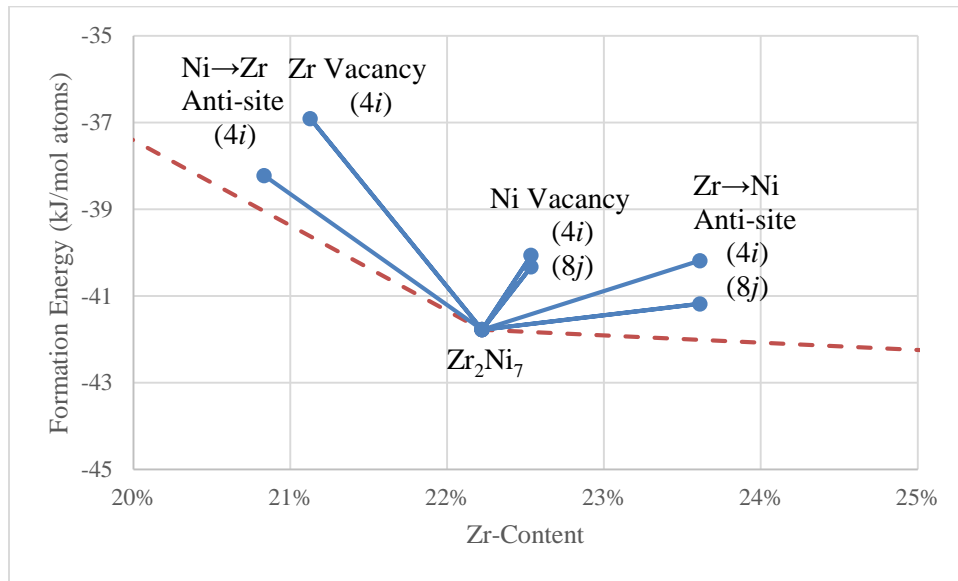
Figure 6. Formation energies for Zr₂Ni₇ and its point defects with tie lines

3.3.2 *Theoretical Effective Formation Energies*

The theoretical defect concentrations for Zr₂Ni₇ phase at 1000°C are plotted as functions of Zr-content for stoichiometric and theoretical off-stoichiometric compositions in Figure 7. Stoichiometric Zr₂Ni₇ phase at 1000°C is dominated by Ni vacancies and Ni→Zr anti-site defects at an approximately 3:1 ratio of total vacancies to total anti-sites. Theoretical Zr-rich compositions promote more defects on the Ni sublattice, but in contrast to Zr-rich Zr₇Ni₁₀ phase, the Zr→Ni anti-site defects overtake the Ni vacancies. Ni-rich compositions theoretically promote defects on the Zr sublattice, with Ni→Zr anti-site defects also dominating in this

theoretical Ni-rich phase. Zr vacancies increase on the Ni-rich side, but again, the concentration does not approach the concentrations of the other defects.
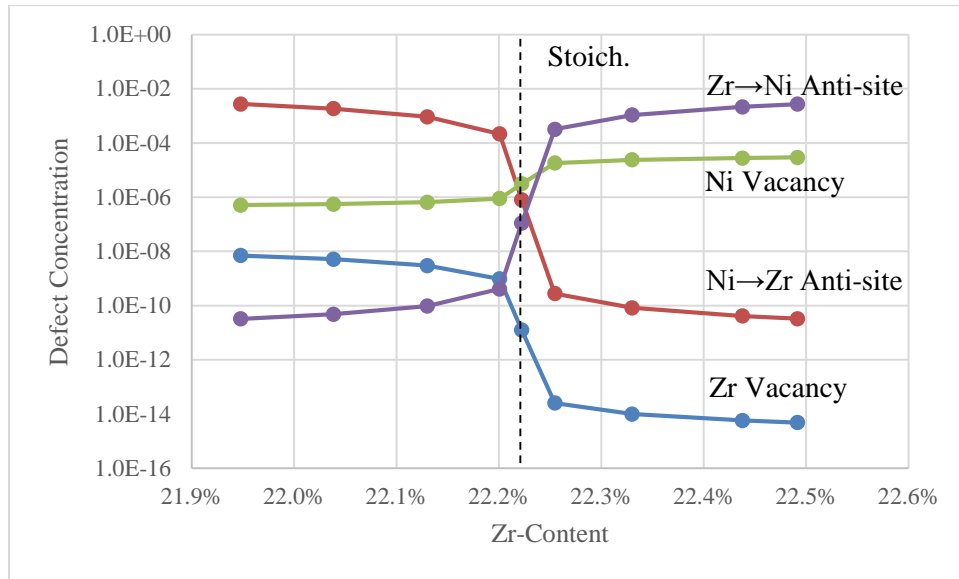
Figure 7. Theoretical defect concentrations for Zr₂Ni₇ at 1000°C

The weighted theoretical effective formation energies for the respective point defects at 1000°C are tabulated in Table 4 and define the relative ease for which the defects can form. The effective formation energies for the defects are consistent with the defect concentration trends observed in Figure 7 with Ni vacancies showing the lowest effective formation energy at stoichiometry.

Table 4. Theoretical effective formation energies for point defects in Zr₂Ni₇ at 1000°C

	ΔH_v^{α} (eV)	ΔH_v^{β} (eV)	ΔH_B^{α} (eV)	ΔH_A^{β} (eV)
Ni-rich	1.89	1.55	0.48	2.63
Stoich.	2.59	1.36	1.37	1.73
Zr-rich	3.45	1.11	2.48	0.63

3.4 Discussion

Theoretical point defect concentrations and effective formation energies of the defects were calculated for Zr_7Ni_{10} and Zr_2Ni_7 systems at 1000°C. Experimentally, Zr_7Ni_{10} shows a small solubility window on the Zr-rich side, and Zr_2Ni_7 has no solubility window. The statistical mechanics model indicates that at stoichiometry, Zr_7Ni_{10} phase tends to form Ni vacancies and Ni→Zr anti-site defects in a 2.4:1 ratio, while Zr_2Ni_7 possibly forms a more complicated complex of 3 Ni vacancies with 1 anti-site defect (Ni→Zr predominant by a ratio of 7:1) to maintain stoichiometry. Zr-rich compositions show a dominance of Ni vacancies in Zr_7Ni_{10} phase, while Zr_2Ni_7 phase show a theoretical preference for Zr→Ni anti-site defects. Theoretical Ni-rich compositions show a preference for Ni→Zr anti-site defects for both phases. In general, it is easier to form defects in Zr_7Ni_{10} phase than Zr_2Ni_7 phase, due to the lower effective formation energies. While the model neglects the effects of the heat of mixing, entropy, vibrational energy and defect interaction on the free energy of each of the possible phases that are needed to draw a more solid conclusion regarding the solubility windows of the two compounds, the DFT formation energies clearly show Zr_7Ni_{10} phase to be more stable than Zr_2Ni_7 phase. This observation indicates that it is more likely for defected Zr_7Ni_{10} structures to form and to contribute to a window of solubility, which does not contradict with reported experimental literature. However, it is more difficult to discern Zr-rich favorability over Ni-rich favorability in Zr_7Ni_{10} phase computationally with the current study.

3.4.1   *Sensitivity Analysis*

A sensitivity analysis is performed to understand the limits of the model given the assumptions used in this study. Deviations in energy between defects on particular Wyckoff

positions can range from 0.001 eV to 1.0 eV. Because multiple sites are taken into account in the statistical mechanics model, this tempers the deviations in the defect concentrations and effective defect formation energies to a degree. Deviations on the order of 0.001 eV appear to have negligible effect on the concentrations and effective formation energies. Deviations on the order of 1.0 eV showing higher energies also have negligible effect; however, when the deviations show lower energies, they can shift effective formation energies lower by 0.7 eV. This can have a dramatic effect on the defect models and on the conclusions that are drawn from them. While preliminary calculations indicate that the neglected $4a$ Zr and $8f$ Zr sites do not have large energy deviations from $8e$ Zr sites, the possibility of lower energy sites and their effect on the formation of defects must be kept in mind when analyzing the defect models presented in this study.

3.4.2 Hydrogen-Assisted Phase Transition in Zr_7Ni_{10}

Experimentally, orthorhombic Zr_7Ni_{10} phase undergoes phase transformation after hydrogenation to form the metastable tetragonal phase [6, 19, 46]. DFT cell optimization of a perfect unit cell yields a near tetragonal structure to have the lowest energy at the ground state (0 K, 0 bar); however, cell optimizations of defected structures yield more orthorhombic phases, as shown in Table 5. While a perfect tetragonal structure shows lower internal energy compared to defected structures, entropic contributions to the free energy likely raises the free energy of the tetragonal structure (higher symmetry yields higher entropy) above the free energy of the defected orthorhombic structure. This suggests that the volume expansion and contraction associated with hydrogenation can change the nature of the defects in Zr_7Ni_{10} to access to the metastable tetragonal phase in experiment, and this can have implications in the design of hydrogen storage alloys.

Table 5. Lattice parameters of Zr_7Ni_{10} and defected structures calculated by DFT

	Perfect Crystal	Zr Vac. (8*d*)	Zr Vac. (8*e*)	Ni→Zr (8*d*)	Ni→Zr (8*e*)	Ni Vac. (16*g*)	Zr→Ni (16*g*)
a (Å)	12.418	12.441	12.335	12.416	12.365	12.376	12.456
b (Å)	9.179	9.136	9.142	9.133	9.135	9.167	9.205
c (Å)	9.180	9.135	9.154	9.138	9.152	9.170	9.234

Comparison of the defected lattice parameters to orthorhombic lattice parameters from experiment suggests that the calculated lattice parameters have a slight over-prediction in *a* and slight under-prediction in *c*. Ni vacancies and Ni→Zr anti-sites appear to help shrink the unit cell, particularly in the *a* direction. Zr→Ni anti-site defects, which is calculated to appear in small quantities at stoichiometry, help expand the unit cell, particularly in the *c* direction.

3.4.3 Zr_7Ni_{10} and Zr_2Ni_7 in Nickel-Metal Hydride Batteries

Secondary phases such as Zr_7Ni_{10} and Zr_2Ni_7 have been shown to enhance electrochemical activity in Laves phase-based Ni/MH battery negative electrodes [3, 4, 6, 7]. As pure phases, Zr_7Ni_{10} shows good hydrogen storage capability, but has deficiencies in reversibility and kinetics, while Zr_2Ni_7 shows smaller hydrogen storage capability, but has excellent reversibility and kinetics [6, 8, 53].   The relative stability of the compounds and the types of point defects can have an effect on the transport properties [9]. For example, vacancies tend to act as hydrogen traps in α-Fe metals [54], which can affect hydrogen reversibility and diffusion rates. While both Zr_7Ni_{10} and Zr_2Ni_7 phases show vacancies to be the predominant defect model in the two phases, vacancy defect concentrations in Zr_2Ni_7 phase at 1000°C is ~50 times smaller than in Zr_7Ni_{10}. This can explain the low reversibility and low diffusion rates in Zr_7Ni_{10} compared to Zr_2Ni_7.

While there is a small solubility window for Zr-rich Zr_7Ni_{10} compounds, modifiers can be added to the composition to engineer the properties of the alloys for better electrochemical performance. Cu is soluble up to 6% at. in Zr_7Ni_{10} [16], and Ti up to 15% at. has been shown to improve the diffusion and high-rate dischargeability without sacrificing capacity [6]. Modifiers have a role in changing the nature of the defects in materials, which can have a consequential effect on electrochemical performance. Small amounts of Nd in multi-element AB2 MH alloys, promote the formation of Zr-Ni phases, showing A/B stoichiometry of up to 0.74 (42.5% at. A elements), while improving the HRD and low-temperature characteristics [55]. It would be of interest to see how Ti and other modifiers change the nature of the defects in Zr_7Ni_{10} using the presented computational defect models and whether it confirms lowering the concentrations of vacancy defects. Also of interest are modifiers that promote Zr→Ni anti-site defects, which would expand the unit cell and possibly improve hydrogen storage capacity [56].

Defects also have an effect on the mechanical properties of the alloys (mainly hardness and ductility), which can affect both the fabrication process and cycle stability against particle pulverization. For example, off-stoichiometric anti-site defects have been shown to improve the hardness of Laves phase alloys [11]. The anti-site defects lower the atomic packing factor to enhance deformability and may also have an effect on the cycling capability in Zr_7Ni_{10}. Zr_7Ni_{10} with higher concentrations of vacancy defects shows high hysteresis in gaseous phase pressure-concentration-temperature analysis [53], which is correlated to poorer cycle life [57], whereas Zr_2Ni_7 with lower concentrations of vacancies shows no hysteresis. Further understanding of the defects that occur in Ni/MH battery materials allows researchers to better engineering their properties.

This study of Zr-Ni-based materials shows a consistent correlation between materials calculated to theoretically have higher concentrations of vacancy defects with the materials that demonstrate poorer absorption/desorption kinetics and hysteresis characteristics in electrochemical experiments. These results are also consistent with the experimental studies that that quantify the effect that point defects have on these specific properties in other intermetallic compounds. Constitutional point defects demonstrably add another dimension in which Ni/MH negative electrode active materials can be studied, as seen in the point defect studies in Laves phase AB_2 materials [11, 14, 23, 24]. While the results of this study do not offer specific pathways to promote the formation of anti-site defects over vacancy defects in Ni/MH negative electrode active materials to improve their performance, it does suggest that the potential for increased disorder and complexity can further propagate synergetic effects that have long been observed in these materials. Ternary alloy defect models can also be built on this binary model to look at the effect of a modifier in A_xB_{1-x} phases, such as Ti in Zr_7Ni_{10} phase [6], and that may offer suggestions for modifiers that could promote anti-site defects.

3.5 Conclusion

Defect models for Zr_7Ni_{10} and Zr_2Ni_7 intermetallic phases were calculated from first-principles using DFT and statistical mechanics to understand the possible roles that point defects have on the performance of Zr-Ni based active negative electrode materials in Ni/MH batteries. DFT calculations confirm that Zr_7Ni_{10} phase structure has space group *Cmca* symmetry in the ground state. DFT formation energies show that the defect structures investigated have higher energies than the perfectly crystalline structures. The defect structures also lie higher in energy than the tie lines to neighboring structures. The statistical mechanics model at 1000°C indicates

that at stoichiometry, Zr_7Ni_{10} phase tends to form Ni vacancies and Ni$\rightarrow$Zr anti-site defects in a 2.4:1 ratio, while Zr_2Ni_7 possibly forms a more complicated complex of 3 Ni vacancies with 1 anti-site defect (Ni$\rightarrow$Zr predominant by a ratio of 7:1) to maintain stoichiometry. Zr vacancies appear almost negligible in both Zr_7Ni_{10} and Zr_2Ni_7 compounds. In general, it is easier to form defects in Zr_7Ni_{10} phase than Zr_2Ni_7 phase, due to the lower effective formation energies, which may give an indication to why there is a solubility window for Zr_7Ni_{10} phase but not for Zr_2Ni_7 phase. The dominance of Ni vacancy defects calculated for stoichiometric and Zr-rich Zr_7Ni_{10} phase and the propensity for vacancies to trap hydrogen also supports the poor diffusion behavior observed experimentally. Modifiers to promote anti-site defects over vacancy defects may result in better transport properties as well as cycling behavior, and would be of interest for future work. First, more resources to remove the limiting assumptions in the point defect models would need to be explored, but the point defect models in this work offer a starting point to better understand the constitutional defects in Ni/MH battery materials, particularly in Zr_7Ni_{10} and Zr_2Ni_7 phases, enabling researchers to engineer better and more robust batteries.

REFERENCES

[1]   News available online.

http://news.panasonic.com/press/news/official.data/data.dir/2014/02/en140213-

3/en140213-3.html

[2]   K. Young, D. Wong, T. Ouchi, B. Huang, B. Reichman, Electrochimica Acta 174 (2015)

815-825.

[3]   J.-M. Joubert, M. Latroche, A. Percheron-Guégan, J. Bouet, Journal of Alloys and

Compounds 240 (1996) 219-228.

[4]   K. Young, J. Nei, T. Ouchi, M. Fetcenko, Journal of Alloys and Compounds 509 (2011)

2277-2284.

[5]   S.R. Ovshinsky, M.A. Fetcenko, J. Ross, Science 260 (1993) 176-181.

[6]   K. Young, T. Ouchi, Y. Liu, B. Reichman, W. Mays, M. Fetcenko, Journal of Alloys and

Compounds 480 (2009) 521-528.

[7]   K. Young, T. Ouchi, M.A. Fetcenko, W. Mays, B. Reichman, International Journal of

Hydrogen Energy 34 (2009) 8695-8706.

[8]   M. Young, S. Chang, K. Young, J. Nei, Journal of Alloys and Compounds 580 (2013)

S171-S174.

[9]   S.M. Myers, M.I. Baskes, H.K. Birnbaum, J.W. Corbett, G.G. DeLeo, S.K. Estreicher,

E.E. Haller, P. Jena, N.M. Johnson, R. Kirchheim, S.J. Pearton, M.J. Stavola, Reviews of

Modern Physics 64 (1992) 559-617.

[10]   K.C. Chen, E.J. Peterson, D.J. Thoma, Intermetallics 9 (2001) 771-783.

[11]   K.C. Chen, F. Chu, P.G. Kotula, D. Thoma, Intermetallics 9 (2001) 785-798.

35

[12] A. Züttel, Materials Today 6 (2003) 24-33.

[13] K. Young, Stoichiometry in Inter-Metallic Compounds for Hydrogen Storage Applications, INTECH Open Access Publisher, 2012.

[14] F. Stein, M. Palm, G. Sauthoff, Intermetallics 12 (2004) 713-720.

[15] M. Kirkpatrick, J. Smith, W. Larsen, Acta Crystallographica 15 (1962) 894-903.

[16] J. Glimois, P. Forey, J. Feron, C. Becle, Journal of the Less-Common Metals 78 (1981) 45-50.

[17] J.-M. Joubert, R. Cerný, K. Yvon, M. Latroche, A. Percheron-Guégan, Acta Crystallographica Section C: Crystal Structure Communications 53 (1997) 1536-1538.

[18] P. Nash, C.S. Jayanth, Bulletin of Alloy Phase Diagrams 5 (1984) 144-148.

[19] H. Takeshita, S. Kondo, H. Miyamura, N. Takeichi, N. Kuriyama, T. Oishi, Journal of Alloys and Compounds 376 (2004) 268-274.

[20] H. Okamoto, Journal of Phase Equilibria and Diffusion 28 (2007) 409-409.

[21] J. Mayer, C. Elsasser, M. Fahnle, Physica Status Solidi B-Basic Research 191 (1995) 283-298.

[22] J. Mayer, M. Fahnle, Acta Materialia 45 (1997) 2207-2211.

[23] J. Zhu, L. Pike, C. Liu, P. Liaw, Acta Materialia 47 (1999) 2003-2018.

[24] J. Zhu, C. Liu, Acta Materialia 48 (2000) 2339-2347.

[25] J.W. Christian, The Theory of Transformations in Metals and Alloys, Newnes, 2002.

[26] I. Kovács, H. El Sayed, Journal of Materials Science 11 (1976) 529-559.

[27] T. Yamamoto, H. Inui, M. Yamaguchi, Intermetallics 9 (2001) 987-991.

[28] P. Notten, R. Einerhand, J. Daams, Journal of alloys and compounds 210 (1994) 221-232.

[29]   J. Bernardini, C. Lexcellent, L. Daróczi, D. Beke, Philosophical Magazine 83 (2003) 329-338.

[30]   R.M. Martin, Electronic structure: Basic Theory and Practical Methods, Cambridge University Press, 2004.

[31]   F. Jensen, Introduction to Computational Chemistry, John Wiley & Sons, 2013.

[32]   M. Born, R. Oppenheimer, Annalen der Physik 389 (1927) 457-484.

[33]   P. Hohenberg, W. Kohn, Physical Review 136 (1964) B864.

[34]   W. Kohn, L.J. Sham, Physical Review 140 (1965) A1133.

[35]   P.H.T. Philipsen, E.J. Baerends, Physical Review B 54 (1996) 5326-5333.

[36]   A.D. Becke, Physical Review A 38 (1988) 3098.

[37]   J.P. Perdew, Y. Wang, Physical Review B 33 (1986) 8800-8802.

[38]   J.P. Perdew, Electronic Structure of Solids' 91, Akademie Verlag, Berlin, 1991.

[39]   J.P. Perdew, K. Burke, M. Ernzerhof, Physical Review Letters 77 (1996) 3865-3868.

[40]   M. Rasamny, M. Weinert, G.W. Fernando, R.E. Watson, Physical Review B 64 (2001) 8.

[41]   V. Schott, M. Fahnle, Physica Status Solidi B-Basic Research 204 (1997) 617-624.

[42]   C.L. Fu, Y.Y. Ye, M.H. Yoo, K.M. Ho, Physical Review B 48 (1993) 6712-6715.

[43]   B. Meyer, M. Fahnle, Physical Review B 59 (1999) 6072-6082.

[44]   R. Krachler, H. Ipser, Physical Review B 70 (2004).

[45]   J.M. Lu, Q.M. Hu, L. Wang, Y.J. Li, D.S. Xu, R. Yang, Physical Review B 75 (2007).

[46]   H.T. Takeshita, N. Fujiwara, T. Oishi, D. Noréus, N. Takeichi, N. Kuriyama, Journal of Alloys and Compounds 360 (2003) 250-255.

[47]   K. Momma, F. Izumi, Journal of Applied Crystallography 44 (2011) 1272-1276.

[48] F. Eshelman, J. Smith, Acta Crystallographica Section B: Structural Crystallography and Crystal Chemistry 28 (1972) 1594-1600.

[49] P. Giannozzi, S. Baroni, N. Bonini, M. Calandra, R. Car, C. Cavazzoni, D. Ceresoli, G.L. Chiarotti, M. Cococcioni, I. Dabo, Journal of Physics: Condensed Matter 21 (2009) 395-502.

[50] K.F. Garrity, J.W. Bennett, K.M. Rabe, D. Vanderbilt, Computational Materials Science 81 (2014) 446-452.

[51] M. Methfessel, A.T. Paxton, Physical Review B 40 (1989) 3616-3621.

[52] H.J. Monkhorst, J.D. Pack, Physical Review B 13 (1976) 5188-5192.

[53] J. Joubert, M. Latroche, A. Percheron-Guégan, Journal of Alloys and Compounds 231 (1995) 494-497.

[54] W.A. Counts, C. Wolverton, R. Gibala, Acta Materialia 58 (2010) 4730-4741.

[55] D. Wong, K. Young, J. Nei, L. Wang, K. Ng, Journal of Alloys and Compounds 647 (2015) 507-518.

[56] H. Nakano, S. Wakao, Journal of Alloys and Compounds 231 (1995) 587-593.

[57] Y. Osumi, Suiso Kyuzou Goukin, new ed., AGNE Gijutsu Center, Tokyo, Japan, 1999, p.218.

ABSTRACT

FIRST-PRINCIPLES POINT DEFECT MODELS IN Zr_7Ni_{10} AND Zr_2Ni_7 BINARY INTERMETALLIC COMPOUNDS AND THEIR IMPLICATIONS IN NICKEL-METAL HYDRIDE BATTERIES

by

DIANA F. WONG

August 2015

Advisor: Dr. K.Y. Simon Ng

Major: Chemical Engineering

Degree: Master of Science

Zr-Ni-based alloys as nickel-metal hydride battery anode materials offer low-cost, flexible and tunable battery performance. Zr_7Ni_{10} is an important secondary phase found in multi-phased AB_2 Laves-phase-based metal hydride alloys, and the synergetic effect between the Zr-Ni and the Laves phases allows access to the high hydrogen storage of the Zr-Ni phases despite the lower absorption/desorption kinetics. Zr_7Ni_{10} displays a small solubility window for Zr-rich compositions, while Zr_2Ni_7, with no solubility window, shows poor capacity with good kinetics. Stability of point defects within the crystal structure allows Zr_7Ni_{10} to maintain the same structure at off-stoichiometric compositions, thus it is theorized that defects may play a role in the difference between the electrochemical behaviors in Zr_7Ni_{10} and Zr_2Ni_7. Defect models in Zr_7Ni_{10} and Zr_2Ni_7 compounds computed using a combination of density functional theory and statistical mechanics offer a starting point for understanding the possible roles that point defects have on the performance of Zr-Ni based active negative electrode materials in Ni/MH batteries. Theoretical vacancy and anti-site defect formation energies are calculated and reported for Zr-rich, Ni-rich, and stoichiometric compounds of Zr_7Ni_{10} and Zr_2Ni_7, and the implications of the

defect models on nickel-metal hydride negative electrode active material design and performance are discussed.

AUTOBIOGRAPHICAL STATEMENT

Diana F. Wong graduated summa cum laude from the University of Michigan in Ann Arbor, Michigan with a Bachelor of Science degree in Chemical Engineering. She joined Energy Conversion Devices, Inc. (ECD) in Rochester Hills, Michigan where she helped develop platinum-free fuel cell stacks and integrated test stands and systems. She moved over to ECD's battery division with Ovonic Battery Company (OBC) where she led testing and development activities for metal-hydride-air batteries and lithium-ion cathode materials. She currently works for BASF, which acquired OBC in 2012.